Journal of
Materials Chemistry A

PAPER

View Article Online
View Journal | View Issue

Cite this: *J. Mater. Chem. A*, 2025, **13**, 2187

Mechanistic study on moisture exposure of Ti-based layered oxides for sodium storage applications†

Benoît D. L. Campéon,[ab] Tetsuya Ishikawa,[a] Kuriyama Tomohiro[a] and Naoaki Yabuuchi*[a]

Received 2nd October 2024
Accepted 3rd December 2024

DOI: 10.1039/d4ta07033j

rsc.li/materials-a

The air stability and moisture sensitivity of titanium-based layered negative electrode materials for sodium storage play a critical role in their practical applications for advanced energy storage systems. However, the impact of moisture exposure on the electrochemical performance of these materials, as well as the potential for recovery through post-calcination treatment, remains unexplored. In this study, the impact of reactions with water molecules through exposure to moisture with high relative humidity and water soaking treatment on crystal structures and electrochemical performance in Na cells of titanium-based layered oxides is explored. The exposure to water molecules results in proton insertion associated with ion-exchange of sodium ions and the formation of sodium hydroxide, which further absorbs carbon dioxide. The removal of protons by post-calcination treatment requires relatively higher temperature, but the metastable layered oxides with oxygen vacancies, which show superior sodium storage reversibility, are newly obtained. The possibility of improvement of air stability and its practical reality for sodium battery applications are also discussed through a mechanistic study on moisture exposure of titanium-based electrode materials.

Introduction

Transitioning to renewable energy is crucial to reduce greenhouse gas emissions, combat climate change, and decrease reliance on finite fossil fuels, thus promoting a more sustainable and resilient energy future. The global initiative to advance renewable energy production has underscored the pivotal role of energy storage devices, which are essential for mitigating the intermittency of renewable sources and ensuring grid stability and reliability.[1–7] Layered sodium negative electrode materials with Ti ions have emerged as promising candidates for next-generation energy storage devices due to their abundance, low cost, and lower operating voltage.[8–11] Layered Ti oxides are particularly attractive due to their wide range of compositions, ease of scalable synthesis, and good reversible specific capacity. Unlike carbon materials, especially hard carbon,[12–19] which typically operate near the sodium plating voltage during cycling, layered Ti oxides offer a higher operating voltage than hard carbon and thus improved stability without the risk of sodium deposition.[20–22] These characteristics make layered Ti oxides safer and highly desirable for sodium battery applications, especially those requiring high power density. However, challenges remain, including irreversible phase transitions, suboptimal electrochemical performance, and instability in air and moisture. The ongoing research and development efforts aim to address these issues, seeking to unlock the full potential of layered Ti oxides as an efficient and reliable negative electrode material for sodium batteries.

Previous studies have explored the impact of moisture exposure and soaking on sodium-containing layered oxides with different transition metal ions, especially for positive electrode materials.[23] For instance, Manthiram *et al.* reported the moisture-induced degradation of an O3-$NaNi_{0.7}Mn_{0.15}Co_{0.15}O_2$ positive electrode, resulting in decreased electrochemical performance due to reactions with H_2O and CO_2.[24] In addition, the reaction with moisture results in Na^+/H^+ ion-exchange, and the presence of H^+ in the Na^+ layers leads to the complicated structural evolution of layered sodium-positive electrode materials upon exposure to air and moisture.[25,26] In addition, a recent study by Zuo *et al.* aims to advance the understanding of the interconnections between these complex reactions, particularly the factors influencing the insertion of water molecules into the Na^+ layers and the determinants of the extent of structural transformation.[27] They found that the redox potential for transition metal ions plays a critical role in the air

---

[a] Advanced Chemical Energy Research Center, Institute of Advanced Sciences, Department of Chemistry and Life Science, Yokohama National University, 79-5 Tokiwadai, Hodogaya-ku, Yokohama, Kanagawa 240-8501, Japan. E-mail: yabuuchi-naoaki-pw@ynu.ac.jp

[b] University Grenoble Alpes, University Savoie Mont Blanc, CNRS, Grenoble INP, LEPMI, Grenoble, France

† Electronic supplementary information (ESI) available. See DOI: https://doi.org/10.1039/d4ta07033j

stability of P2-Na_xTmO_2, with higher redox potential leading to improved stability. These studies emphasized the critical importance of moisture stability and highlighted the need for effective strategies to mitigate the detrimental effects of moisture exposure on these materials.

Presently, previous research has provided important insights into the effects of moisture on layered sodium positive electrode materials. However, the knowledge of air stability of layered titanium-based negative electrode materials is limited. Generally, to increase theoretical capacities, titanium layered oxides with Na ions are designed with high sodium deficiency, which would influence moisture reactivity. Therefore, further studies are needed to expand our understanding and find strategies to expedite the practical implementation of layered titanium negative electrode materials for Na battery applications.

In this study, we aim to build upon previous research by systematically studying the effect of exposure to moisture and soaking in water on layered sodium negative electrode materials, specifically focusing on four Ti-based layered phases with different compositions and layered stackings. By comparing the Ti-based layered materials with different layered stacking modes, P2 and P3 phases, as well as examining the impact of layered phases substituted by different metal components, Cr^{3+}, Mg^{2+}, and Li^{+} ions, we seek to gain a comprehensive understanding of the structural and electrochemical changes induced by the presence of moisture. Furthermore, we will explore the potential of calcination as a post-treatment method to recover and enhance the performance of materials exposed to moisture/soaked in water. The outcomes of this study will contribute to the development of moisture-tolerant layered Ti-based layered negative electrode materials and provide valuable insights for the design and optimization of practical sodium-ion battery systems. By elucidating the effects of moisture on these materials and proposing strategies for performance recovery, we aim to advance the field of energy storage and enable the practical implementation of cost-effective sodium-ion batteries in various applications.

Results and discussion

The four Ti-based layered oxides with different chemical compositions and stacking modes examined in this study, namely P2 $Na_{2/3}Cr_{2/3}Ti_{1/3}O_2$ (hereafter denoted as P2-NaCrTiO),[20] P3 $Na_{0.58}Cr_{0.58}Ti_{0.42}O_2$ (P3-NaCrTiO),[28] P2 $Na_{2/3}Cr_{1/3}Mg_{1/2}Ti_{1/2}O_2$ (P2-NaCrMgTiO),[22] and P2 $Na_{0.67}Li_{0.22}Ti_{0.78}O_2$ (P2-NaLiTiO),[29] were synthesized using a methodology described in the Experimental section. Herein, "P2" and "P3" refer to the P2-type and to the P3-type layered structure, respectively, according to the Delmas notation, where "P" denotes a coordination environment for Na ions, where Na ions are found at prismatic

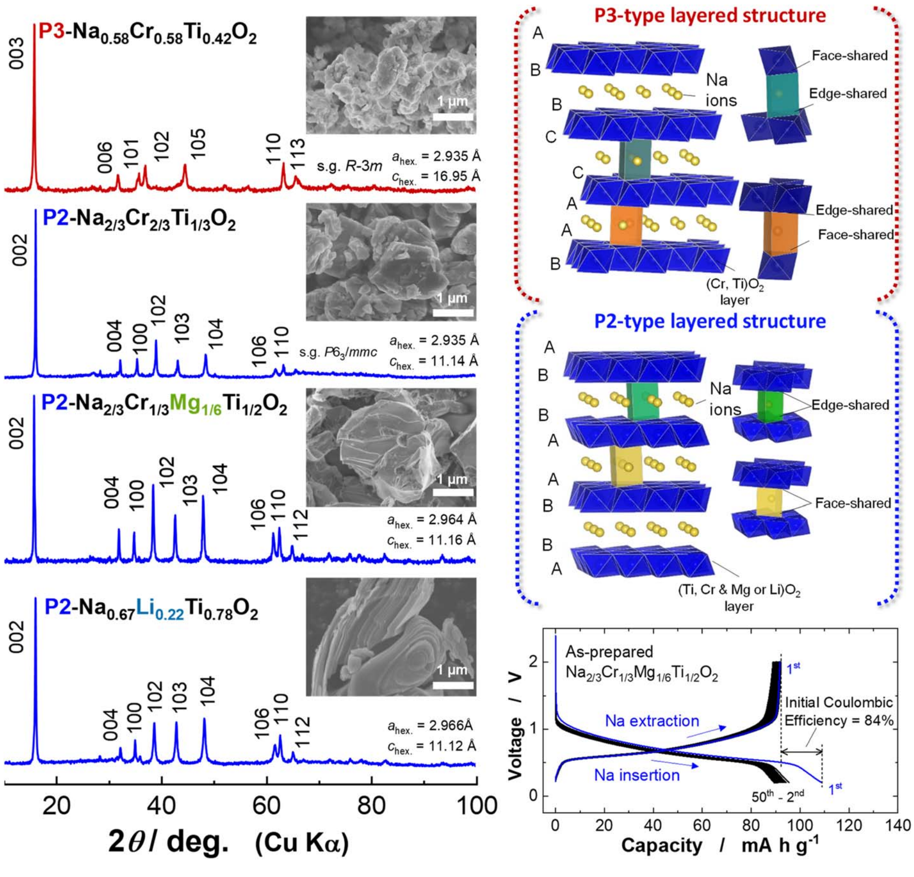

Fig. 1 XRD spectra, SEM images, and the corresponding illustrations of crystal structures for P3 $Na_{0.58}Cr_{0.58}Ti_{0.42}O_2$, P2 $Na_{2/3}Cr_{2/3}Ti_{1/3}O_2$, P2 $Na_{2/3}Cr_{1/3}Mg_{1/6}Ti_{1/2}O_2$, and P2 $Na_{0.67}Li_{0.22}Ti_{0.78}O_2$. Charge/discharge curves of P2 $Na_{2/3}Cr_{1/3}Mg_{1/6}Ti_{1/2}O_2$ stored in a glove box without air exposure is also shown.

sites as illustrated in Fig. 1.[30] The numbers "2" and "3" correspond to the number of transition metal oxide layers in a unit cell. To ensure the preservation of the synthesized samples' integrity and minimize the influence of moisture exposure, the final samples were carefully handled and stored in an argon-filled glovebox. To gain insights into the structural properties of the synthesized samples, X-ray diffraction (XRD) analysis was performed. XRD patterns displayed in Fig. 1 confirm that all target samples were obtained, displaying characteristic P2 diffraction lines for the as-prepared P2-NaCrTiO, P2-NaCrMgTiO, and P2-NaLiTiO, while P3 diffraction lines can be observed for the as-prepared P3-NaCrTiO. The samples display an interlayer distance of about ~5.6 Å. Further morphological characterization was carried out using scanning electron microscopy (SEM), and the results are presented in the insets of Fig. 1. The as-prepared samples have a particle size ranging from micro- to submicro-meter, but it can be noticed that P3 NaCrTiO displays a slightly smaller particle size. This originates from the fact that P3-NaCrTiO is a low temperature phase, and the sample was synthesized at a lower temperature (835 °C), compared with P2-NaCrTiO a high temperature phase synthesized at 1000 °C. A typical example of electrochemical properties of Ti-based layered materials in Na cells is also shown in Fig. 1. The sample stored in the Ar-filled glove box without air exposure shows good reversibility as a negative electrode material. P2-NaCrMgTiO can accommodate 1/3 mol Na ions in the vacant sites between transition metal layers with relatively high initial coulombic efficiency, ~84%, with good cyclability.

To assess the robustness of the prepared materials, moisture exposure and water soaking tests were conducted, as depicted in Fig. 2a. The moisture exposure resistance test involved incubating the powder samples in a chamber at 100% relative humidity (RH) and 20 °C for 5 days. The samples obtained from these tests were labeled as RH P2 NaCrTiO, RH P3 NaCrTiO, RH P2 NaCrMgTiO, and RH P2 NaLiTiO. The monitoring of mass changes before and after the moisture exposure test indicates gravimetric increases of 27, 30, 59, and 71% for P2 NaCrMgTiO, P2 NaLiTiO, P2 NaCrTiO, and P3 NaCrTiO, respectively, foreseeing less water absorption for P2 NaCrMgTiO and P2 NaLiTiO. Structural evaluations of these samples by X-ray diffraction (XRD), reported in Fig. 2b and ESI Fig. S1,† reveal structural changes in RH P3 NaCrTiO and RH P2 NaCrTiO. Specifically, their 003 and 002 diffraction lines are shifted to lower angles, indicating increases in interlayer distances from ~5.6 to ~7.0 Å. This increase suggests that during the moisture exposure resistance test, water molecules are intercalated between metal oxide layers as illustrated in Fig. 2c. Interestingly, RH P2 NaLiTiO shows no shift to lower angles, but new peaks are visible (Fig. 2b and ESI Fig. S1†), indicating that although P2 NaLiTiO is affected by moisture, it maintains its structural integrity in the presence of Li ions. Because these new peaks are found in the regions with higher diffraction angles for the original P2 layered phase (ESI Fig. S1†), this new phase has the same P2 layered structure with shorter lattice parameters, probably originating from partial Na^+/H^+ ion-exchange upon moisture exposure. This process also results in the accumulation of NaOH on the particle surface, and NaOH further reacts with CO_2, leading to the appearance of new peaks for the crystalline phase. This phase is further analyzed in the later section. In addition to the ion-exchange process, as reported by Victor Duffort *et al.*,[31] CO_2 insertion into the crystal lattice of P2 NaLiTiO is also another possibility, which potentially influences the lattice parameter change after the moisture exposure test. Notably, the Mg-substituted sample, P2 NaCrMgTiO, shows no significant structural changes, without the formation of a new phase, during the moisture exposure resistance test, indicating its superior robustness against moisture. Nevertheless, water absorption at the oxide surface and partial ion-exchange cannot be eliminated as discussed in the later section.

Observation of the samples' morphology by scanning electron microscopy (SEM), as reported in ESI Fig. S2 and S3,† indicates no critical changes caused by the moisture exposure test, except for RH P2 NaLiTiO. Additional smaller particles with a needle-like morphology appear, which is consistent with XRD observation. Remarkably, under a high-energy electron beam, these needle-like particles were decomposed, underscoring the need for mild conditions during its characterization. Elemental mapping by energy-dispersive X-ray spectroscopy (EDX) of RH P2 NaLiTiO given in ESI Fig. S4† shows that the Na distribution is richer for these new particles, further supporting the Na^+/H^+ exchange and formation of NaOH on the P2 NaLiTiO surface upon moisture exposure.

Additionally, a water soaking test, as illustrated in Fig. 2a, was conducted by directly immersing the powder samples in distilled water for 3 hours, followed by filtration and vacuum drying at 60 °C. During the soaking test, the pH of solutions increased within 30 minutes above $pH = 10$, which corroborates the presence of basic compounds with Na ions in solutions. The obtained samples preserved their original color and were labeled SK P2 NaCrTiO, SK P3 NaCrTiO, SK P2 NaCrMgTiO, and SK P2 NaLiTiO. In good agreement with the moisture exposure resistance test, the water soaking test confirms the structural instability of P2 NaCrTiO and P3 NaCrTiO, as their interlayer distances reach ~7.0 Å, contrasting with the structural stability of P2 NaCrMgTiO and P2 NaLiTiO. As expected, SK P2 NaLiTiO does not present a peak adjacent to its 002 diffraction line, which corroborates the formation of a crystalline alkaline compound, visualized in ESI Fig. S4,† but it is a water-soluble species and is dissolved in water from the P2 NaLiTiO surface during the water soaking test.[32] The SEM analysis of these samples, reported in Fig. 2d–g and ESI Fig. S2 and S3,† shows clear cracks for all water-soaked samples. It should be noted that only for SK P2 NaCrTiO, these cracks are easily found and visualized due to its interlayer expansion and relatively large particle size, ~1 μm. In agreement with the XRD observation of SK P2 NaLiTiO, the SEM observation indicates that the side product is effectively washed away from its surface during the water soaking test. Indeed, as illustrated in Fig. 2a, water filtered from all samples was dried to obtain white powders, which were labeled EX P2 NaCrTiO, EX P3 NaCrTiO, EX P2 NaCrMgTiO, and EX P2 NaLiTiO. Structural examination *via* XRD analysis of EX P2 NaCrTiO, shown in ESI Fig. S5,† indicates

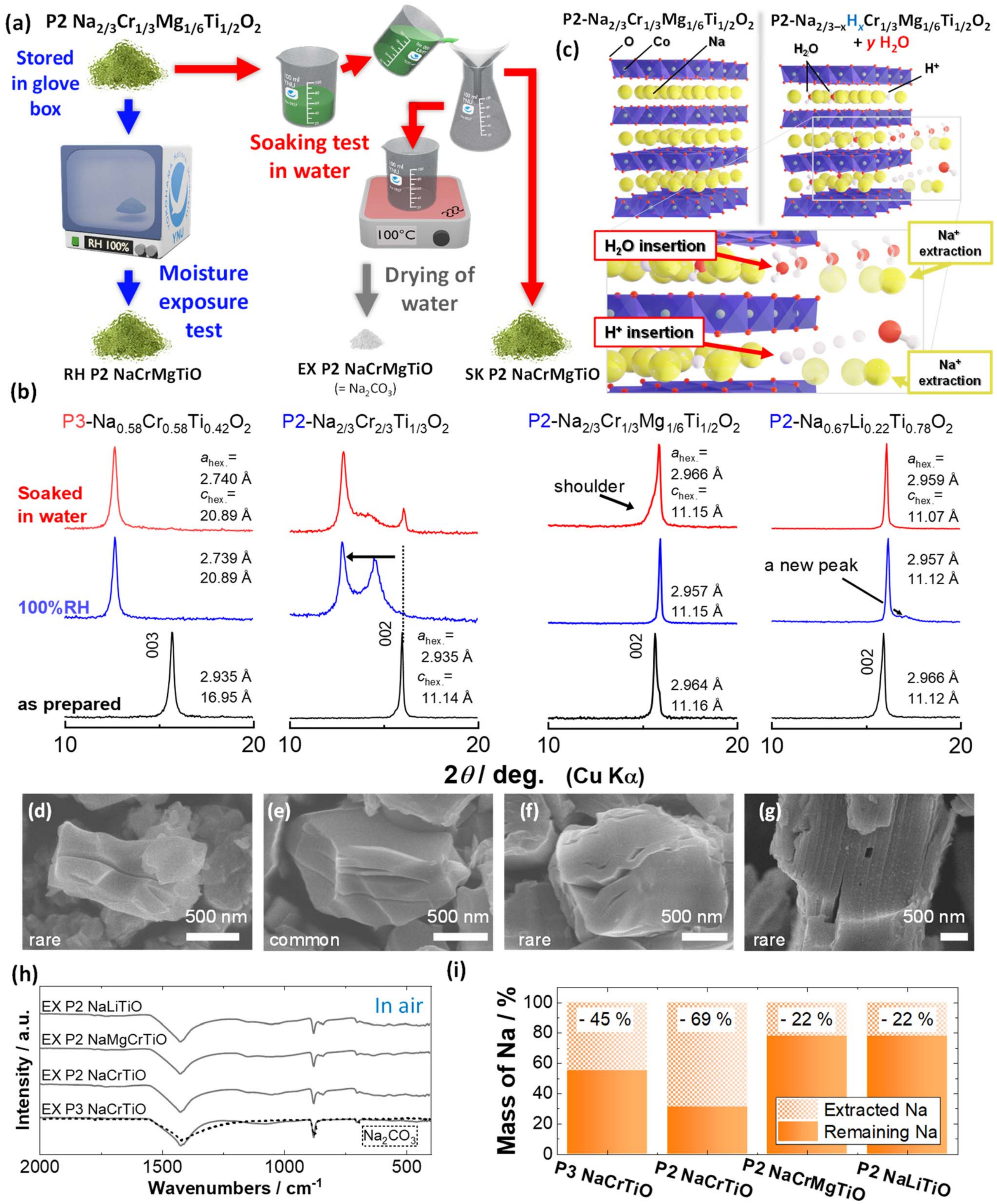

Fig. 2 Water exposure test. (a) A schematic illustration of water soaking and moisture exposure tests, (b) structural characterization *via* XRD, and (c) a scheme for the Na^+/H^+ ion-exchange process. SEM morphological observation of water-soaked (d) P3 $Na_{0.58}Cr_{0.58}Ti_{0.42}O_2$, (e) P2 $Na_{2/3}Cr_{2/3}Ti_{1/3}O_2$, (f) P2 $Na_{2/3}Cr_{1/3}Mg_{1/6}Ti_{1/2}O_2$, and (g) P2 $Na_{0.67}Li_{0.22}Ti_{0.78}O_2$. Characterization of byproducts of the soaking test *via* (h) IR and (i) UV-vis spectroscopy.

that these materials correspond to Na_2CO_3. Attenuated total reflectance Fourier-transform infrared (ATR-FTIR) spectroscopy analysis of these powders (Fig. 2h) reveals that the spectra of all samples show peaks mainly corresponding to Na_2CO_3 (ESI Fig. S6†).[33] In agreement with the above results, it indicates that all samples, including structurally stable P2 NaCrMgTiO and P2 NaLiTiO, undergo Na^+/H^+ exchange upon soaking in water. Assuming that these white powders are mainly composed of Na_2CO_3, the gravimetric analysis indicates that structurally unstable P2 NaCrTiO and P3 NaCrTiO exchange approximately 60 and 33% of their Na^+ ions, while structurally stable P2 NaCrMgTiO and P2 NaLiTiO exchange only 23% and 20% of their Na^+ ions, respectively. Additionally, the filtered water before evaporation was analyzed by ultraviolet-visible (UV-vis) absorption spectroscopy, as shown in ESI Fig. S7† and Fig. 2i. These values were calibrated from the correlation between the aqueous solution absorbance and concentration of NaOH and Na_2CO_3 from UV-vis spectra (ESI Fig. S8†). The analysis of these solutions' concentration observes 69, 45, 23, and 22% Na^+ extracted for P2 NaCrTiO, P3 NaCrTiO, P2 NaCrMgTiO, and P2 NaLiTiO, respectively. These findings align with the ATR-FTIR and UV-vis spectra illustrated in Fig. 2a, indicating that upon exposure to water molecules, Na^+/H^+ exchange proceeds for all samples, but its extent and insertion of water molecules depend on the layered stacking modes and chemical compositions. The extracted Na^+ forms NaOH, resulting in the formation of Na_2CO_3 after CO_2 absorption in air. In the moisture exposure test, the Na_2CO_3 remains on the sample surface, while during soaking in water, Na^+ ions are dissolved in water from the sample surface. Among the tested samples, P2 NaCrMgTiO and P2 NaLiTiO show better air stability with less Na^+/H^+ ion-exchange without H_2O intercalation into the crystal lattice, even though shoulder peaks, which are indicative of partial H_2O insertion, are observed for SK P2 NaCrMgTiO.

To explore recovery routes of water exposed samples by thermal treatment, preliminary thermogravimetry (TG) analysis was conducted. TG curves of the samples after exposure to moisture or soaking in water with their differential curves are shown in Fig. 3a. The results indicate that all water-soaked samples show two mass loss regions, from 50 to 100 °C and from 100 to 600 °C, while all moisture-exposed samples present an additional mass loss region from 500 to 835 °C. All these regions seem to be composed of several peaks, which denotes that the mass loss involves several consecutive mass loss mechanisms during heating. To determine the mechanism involved in each mass loss region, mass spectroscopy analysis was conducted for RH P2 NaLiTiO and RH P2 NaCrMgTiO. The mass spectra (Fig. 3b) indicate that as expected, the first mass loss region, from 50 to 100 °C, corresponds to the removal of H_2O adsorbed on the surface of the material. For RH P2 NaCrTiO and RH P3 NaCrTiO, a more dramatic mass loss is observed, indicating that more moisture is absorbed by those samples. The second region, from 100 to 600 °C, displays formation of different gases for RH P2 NaLiTiO and RH P2 NaCrMgTiO. Indeed, RH P2 NaCrMgTiO mostly releases H_2O in this region, corresponding to the removal of H^+ from its Na layers, which was further confirmed by mass spectroscopy (Fig. 3b). Additionally, RH P2 NaLiTiO releases CO_2 in this region, attesting to the presence and removal of CO_3^{2-} from the transition metal layer of this sodium metal oxide. The third region, from 500 to 835 °C, is characterized by the release of CO_2. This region is only found for moisture-exposed samples, indicating that CO_2 release in this region originates from the decomposition of Na_2CO_3 present on the sample surface. To clarify the role played by CO_2, additional moisture-exposed samples have been prepared in the absence of CO_2. Remarkably, similar to the results previously published for layered sodium positive electrode materials,[34] the mass gain is decreased for all our layered sodium negative electrode materials, Table S1.† However, structural study *via* XRD analysis, presented in Fig. S9,† indicates no clear difference between samples prepared with and without CO_2. TG results obtained for samples exposed to moisture in the absence of CO_2, presented in Fig. 3a, display no third region, confirming that the peak in that region for moisture-exposed samples correspond to the decomposition of Na_2CO_3 present on the sample surface resulting from the reaction between NaOH and CO_2. It is also noted that in the absence of CO_2, all samples exhibit an additional decomposition peak between 500 °C and 600 °C, which could originate from the decomposition of NaOH and/or the reaction of oxides with Na_2O formed by NaOH decomposition in the absence of CO_2. Additionally, RH P2 NaCrTiO and RH P3 NaCrTiO exhibit even stronger Na^+/H^+ exchange because H_2O removal, associated with the elimination of H^+ from the lattice, is expected to proceed in the higher temperature region, ~600 ° C, which is further discussed in the later section. H_2O release at higher temperatures is intensified for both samples.

To further track the structural evolution during the re-calcination process, an XRD study was conducted for the heat-treated samples, as shown in Fig. 3c, S10, and S11.† As foreseen, all the moisture-exposed and water-soaked samples after re-calcination above 600 °C recover close to their original structures and similar interlayer distances without impurities. However, peak widths are broadened compared with the as-prepared samples. Na^+/H^+ ion-exchange samples, for instance, $Na_{2/3-y}H_yCr_{1/3}Mg_{1/2}Ti_{1/2}O_2$, are formed, and H^+ removal from $Cr_{1/3}Mg_{1/2}Ti_{1/2}O_2$ is expected to be achieved with oxygen extraction from the crystal lattice, leading to the formation of a metastable phase with oxygen vacancies, *i.e.*, $Na_{2/3-y}Cr_{1/3}Mg_{1/2}Ti_{1/2}O_{2-y/2} + y/2H_2O.\cdot CO_2$ insertion into the lattice and the loss of CO_3^{2-} ions on heating would influence phase transition processes. Indeed, for the P2 NaLiTiO system, the re-calcination is also accompanied by the presence of an additional peak at 45.0°. The formation of a new phase is also clearly visualized as changes in the particle morphology in Fig. S2 and S3.† An attempt to identify any differences in chemical compositions by EDX mapping is unsuccessful, and no visible atomic distribution difference is observed, as shown in Fig. S4.† When the re-calcination temperature is further increased above 835 °C for moisture-exposed samples, the same diffraction patterns with the as-prepared samples are observed, indicating that metastable phases formed by the loss of H^+/CO_3^{2-} on heating react with Na^+ ions formed by Na_2CO_3 decomposition. In contrast, a different trend is noted for water-soaked samples, and a new

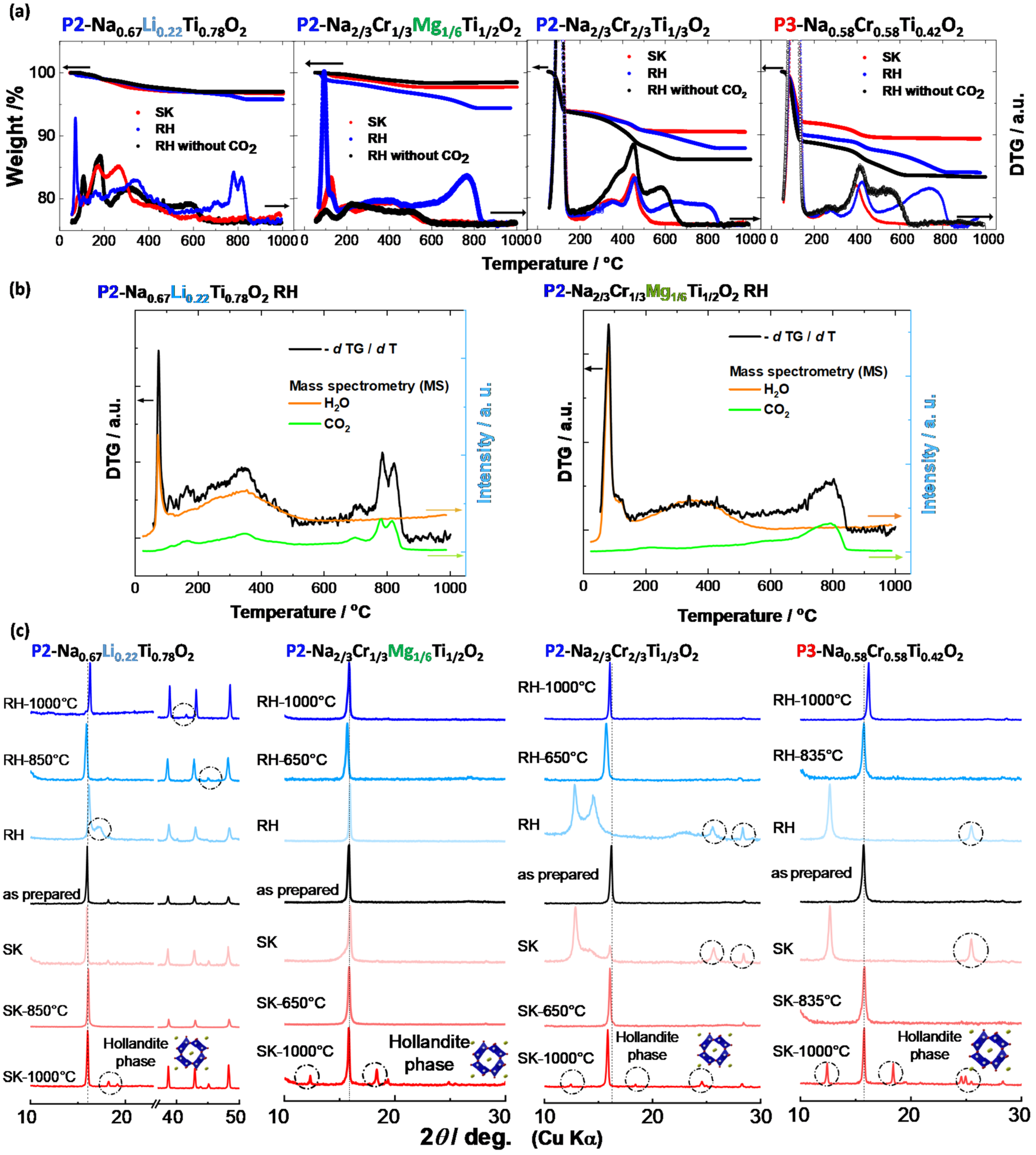

Fig. 3 Calcination after air exposure and water-soaking test. (a) TG curves with differential curves (−dTG (mass of samples)/d*T*) of all samples and (b) corresponding differential TG curves and GC-MS spectra of generated gas for P2 $Na_{2/3}Cr_{1/3}Mg_{1/6}Ti_{1/2}O_2$ and P2 $Na_{0.67}Li_{0.22}Ti_{0.78}O_2$, and (c) structural evolution monitoring *via* XRD analysis.

phase is formed after heating at 1000 °C. These peaks can be assigned to a hollandite phase, which is a typical sodium-deficient phase, for instance $Na_{2/5}Cr_{2/5}Ti_{3/5}O_2$.[35]

These studies identify two distinct thermal recovery pathways, as depicted in Fig. 4, one for moisture-exposed samples and another for water-soaked samples. As observed previously, both moisture exposure and soaking in water lead to Na^+/H^+ exchange in Ti-based layered materials, resulting in the formation of partially desodiated and protonated samples, such as $Na_{2/3-x}H_xCr_{1/3}Mg_{1/6}Ti_{1/2}O_2$ coupled with NaOH formation. However, moisture exposure results in the accumulation of Na_2CO_3 on the surface, whereas soaking in water leads to the

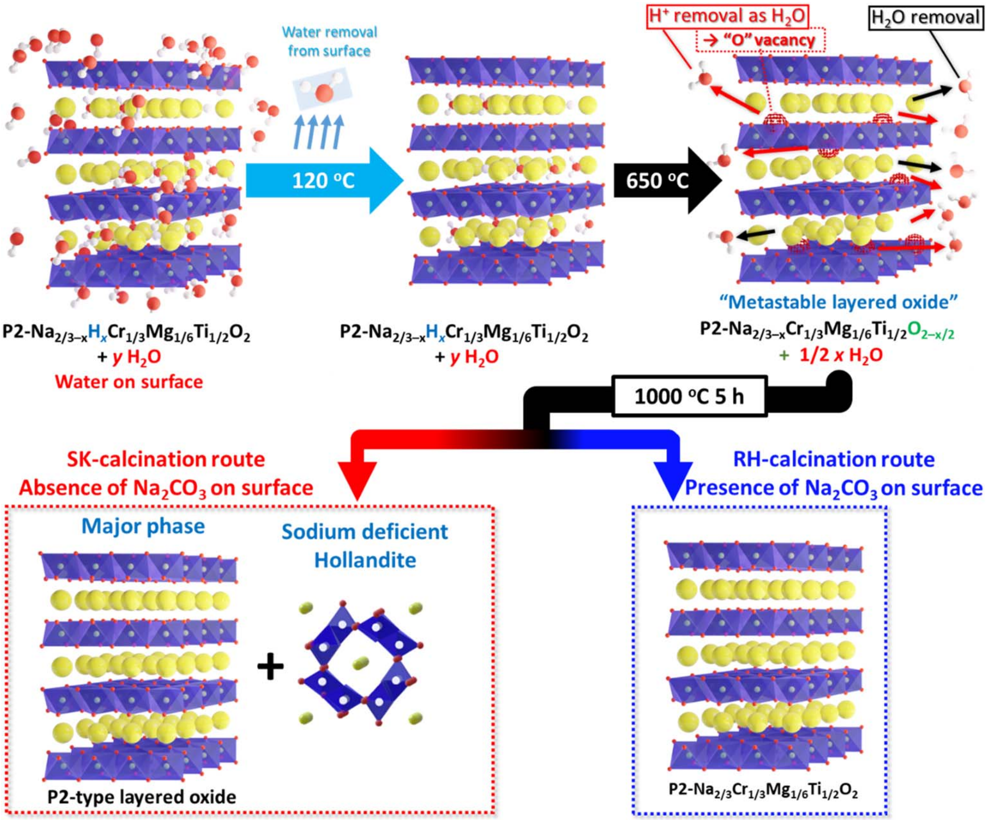

Fig. 4 A schematic illustration of proposed structural changes upon calcination after the water soaking or moisture exposure test.

dissolution of NaOH in the solution. The extracted Na^+ ions are further separated from the sample *via* filtration. For moisture-exposed samples, upon calcination, intercalated H^+ is released as H_2O couples with oxygen vacancy formation in the framework structure, forming metastable phases. The phases obtained by H^+ extraction further reacts with Na_2CO_3, regenerating the as-prepared phase, P2 $Na_{2/3}Cr_{1/3}Mg_{1/6}Ti_{1/2}O_2$, as illustrated in Fig. 4. For water-soaked samples, extracted Na^+ is lost by filtration; therefore, upon calcination, metastable phases obtained by H^+ extraction decompose on further heating to 1000 °C, leading to the formation of a P2-type layered oxide and a non-layered sodium-deficient phase with Ti ions.

Finally, to assess the robustness of the Ti-based layered electrode materials against moisture exposure and soaking in water, electrochemical characterization was performed using a half-cell configuration with metallic sodium as the counter electrode in 1.0 mol dm^{-3} $NaPF_6$ dissolved in propylene carbonate used as the electrolyte and an electrode composed of active materials, acetylene black, and the poly(acrylonitrile)-grafted poly(vinyl alcohol) copolymer (PVA-*g*-PAN).[36] Note that poly(vinylidene fluoride) (PVdF), which is often used as a binder for battery applications, easily shows gelation when an alkaline residue is present in the sample, and therefore it is difficult to use PVdF as a binder for the moisture-exposed samples.[37–39] Galvanostatic charge/discharge curves in the first cycle, as presented in Fig. 5a, show that both moisture-exposed and water-soaked samples exhibit lower discharge (oxidation) capacities compared to the pristine samples stored in the Ar-filled glove box. This capacity loss is also accompanied by a decrease in the initial coulombic efficiency (ICE). Interestingly, the moisture exposure test appears more detrimental to the electrode materials compared to the water soaking test. This outcome could be attributed to the fact that the surface of the samples is damaged by the formation of NaOH and the accumulation of Na_2CO_3 during moisture exposure, which forms the high resistance layer for Na^+ exchange between oxides and electrolyte solutions. Among the samples, P2 $Na_{2/3}Cr_{1/3}Mg_{1/6}Ti_{1/2}O_2$ shows nearly unchanged capacity retention after both moisture exposure and water soaking tests (Fig. 5b). Subsequently, P2 NaCrTiO, P3 NaCrTiO, P2 NaCrMgTiO, and P2 NaLiTiO were recalcined at 650, 835, 650, and 850 °C, respectively. For the water-soaked samples, recalcination restores the ICE; however, the reversible capacity is reduced because of the surface damage. The formation of a hollandite phase is also noted for P2 NaLiTiO, which reduces the reversible capacity as electrode materials. Nevertheless, recalcined P2 $Na_{2/3}Cr_{1/3}Mg_{1/6}Ti_{1/2}O_2$ after soaking in water exhibits a higher reversible capacity, >100 mA h g^{-1}, compared with the as-prepared sample, indicating that the sodium-deficient metastable phase, P2 $Na_{2/3-x}Cr_{1/3}Mg_{1/6}Ti_{1/2}O_{2-x/2}$, shows superior reversibility without surface degradation. The increase in the vacant sites after H^+ removal from the layered oxides results in a larger reversible capacity as electrode materials. For the moisture-exposed samples, recalcination partially restores the original reversible capacity for P2 NaCrTiO and completely restores it for P3 NaCrTiO and P2 NaCrMgTiO, as shown in Fig. 5, where recalcination recovers the initial

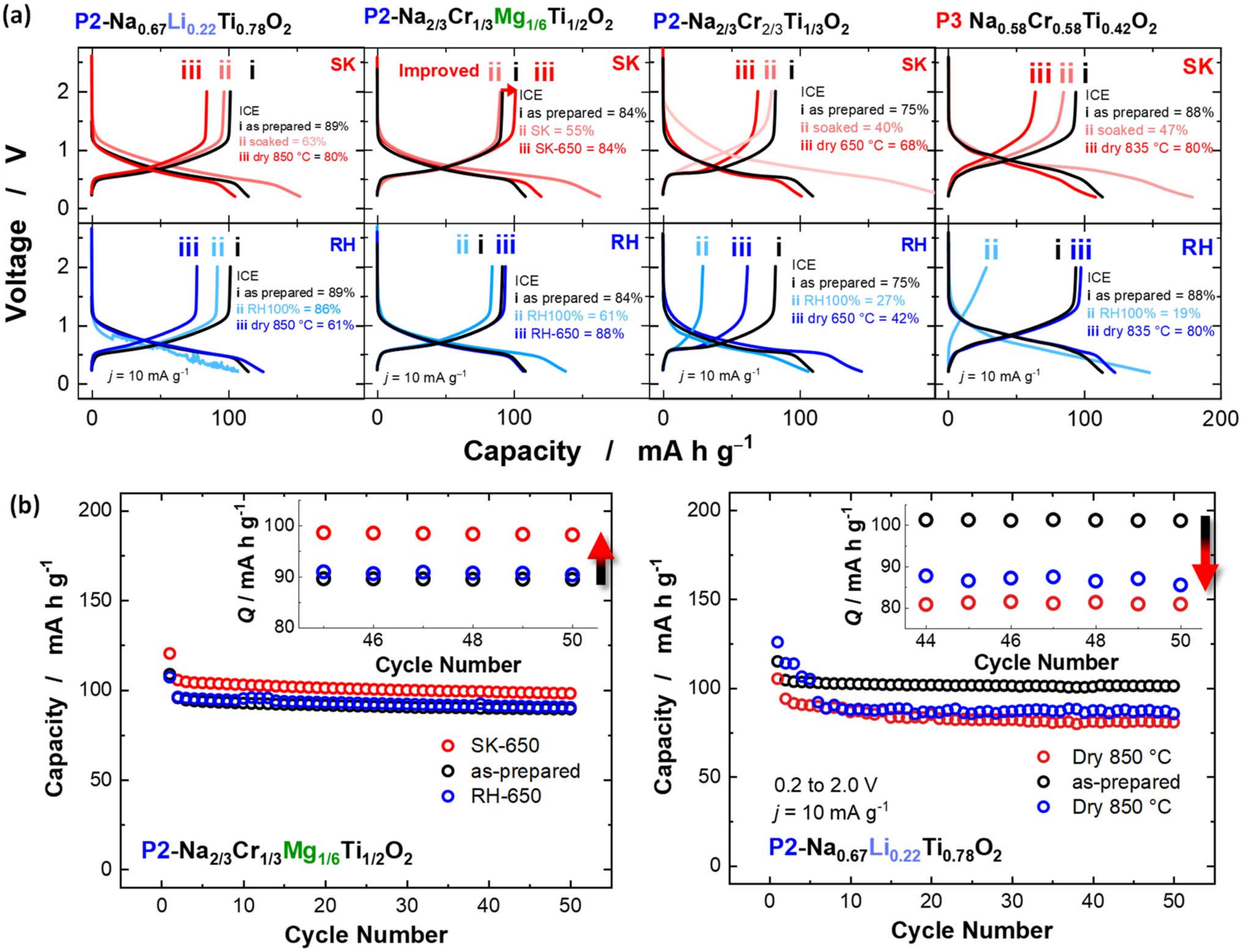

Fig. 5 Electrochemical characterization. P3 $Na_{0.58}Cr_{0.58}Ti_{0.42}O_2$, P2 $Na_{2/3}Cr_{2/3}Ti_{1/3}O_2$, P2 $Na_{2/3}Cr_{1/3}Mg_{1/6}Ti_{1/2}O_2$, and P2 $Na_{0.67}Li_{0.22}Ti_{0.78}O_2$ before/after soaking in water/moisture exposure and after re-calcination. (a) First charge/discharge cycles at a rate of 10 mA g^{-1} and (b) capacity retention for consecutive 50 cycles.

crystal structure for these samples. However, for P2 NaLiTiO, recalcination of the moisture-exposed and water-soaked samples leads to capacity decay, which is consistent with the fact that a new phase is formed after recalcination (Fig. 3c). Upon cycling, as presented in Fig. 5b, S12, and S13,† the recovery of moisture-exposed samples shows promising results for all chromium/titanium-based systems, especially for the Mg-substituted sample, with the original capacity and CE maintained during the first 50 cycles. In contrast, P2 NaLiTiO exhibits only 90% of its original capacity associated with the phase segregation as mentioned above. Although the degradation by moisture exposure is a practical problem for Ti-based layered materials, P2 NaCrMgTiO shows better stability and recovery for electrode performance after re-calcination, which is a superior characteristic for battery applications.

Conclusions

This study systematically explored the structural robustness and electrochemical performance of various titanium-based layered oxides for Na storage applications subjected to moisture tolerance. The materials studied, including P2 NaCrTiO, P3 NaCrTiO, P2 NaCrMgTiO, and P2 NaLiTiO, exhibited distinct responses to moisture and carbon dioxide exposure. During the moisture-exposure test, all samples exhibited water absorption and surface coverage by Na_2CO_3 coupled with the partial Na^+/H^+ ion-exchange reaction. However, the partially Mg-substituted sample, P2 NaCrMgTiO, and Li-substituted sample, P2 NaLiTiO, demonstrated superior structural stability with minimal interlayer expansion without H_2O intercalation into the crystal lattice, in contrast to P2 NaCrTiO and P3 NaCrTiO, which showed increased interlayer distances due to H_2O intercalation and the formation of hydrate phases. These structural changes adversely impacted their electrochemical performance, leading to capacity loss and reduced CE during cycling. Nevertheless, the recalcination treatment effectively restored the crystal structure and partially recovered the electrochemical properties. On the other hand, water soaking tests resulted in distinct behavior. A critical factor complicating the recovery of water-soaked samples is the loss of Na^+ ions by filtration during the soaking test. This absence of Na^+ ions prevented efficient recrystallization during calcination, thereby hindering the restoration of electrochemical properties. Among the tested samples, P2 NaCrMgTiO exhibited exceptional stability and even better reversible capacity after recalcination compared with the as-prepared sample. This fact originated from the formation of a Na-deficient metastable phase, P2-$Na_{2/3-x}Cr_{1/3}Mg_{1/6}Ti_{1/2}O_{2-x/2}$, obtained by H^+ removal coupled with oxygen vacancy formation. Overall, the results have confirmed that titanium-based layered oxides are prone to instability when exposed to air due to Na^+/H^+ ion-exchange and NaOH formation. However, partial Mg substitution has proven to be an efficient strategy to enhance the stability against moisture. Future research efforts could focus on optimizing material formulations to further mitigate structural changes upon exposure to moisture and carbon dioxide, thereby enhancing the long-term cycling stability and performance of sodium-ion batteries fabricated under ambient air conditions.

Experimental section

P2 $Na_{2/3}Cr_{2/3}Ti_{1/3}O_2$ synthesis

P2 $Na_{2/3}Cr_{2/3}Ti_{1/3}O_2$ was prepared from Na_2CO_3 (99.5%, Wako Pure Chemical Industries, Ltd), Cr_2O_3 (98%, Wako Pure Chemical Industries, Ltd), and anatase TiO_2 (98.5%, Wako Pure Chemical Industries, Ltd). The precursors were thoroughly mixed by wet ball-milling with a ZrO_2 pot (40 mL) and balls (27 g) with ethanol (20 mL) at 300 rpm for 5 h in air. Afterward, the obtained powder was pressed into a pellet at a pressure of 15 MPa and heated in a tube furnace at 1000 °C under an argon atmosphere for 5 hours with Cu foil to avoid oxidation by leaked air.[40] Finally, the sample was hand-milled to obtain a powder before electrode preparation. The as-obtained sample showed a typical green color and was stored in argon. In general, 1.0 g of sample was obtained after calcination.

P3 $Na_{0.58}Cr_{0.58}Ti_{0.42}O_2$ synthesis

P3 $Na_{0.58}Cr_{0.58}Ti_{0.42}O_2$ was prepared from Na_2CO_3 (99.5%, Wako Pure Chemical Industries, Ltd), Cr_2O_3 (98%, Wako Pure Chemical Industries, Ltd), and anatase TiO_2 (98.5%, Wako Pure Chemical Industries, Ltd). The precursors were thoroughly mixed by wet ball-milling with a ZrO_2 pot (40 mL) and balls (27 g) with ethanol (20 mL) at 300 rpm for 5 h in air. Afterward, the obtained powder was pressed into a pellet at a pressure of 15 MPa and heated in a tube furnace at 835 °C under an argon atmosphere for 12 hours. The powder displayed a green color.

P2 $Na_{2/3}Cr_{1/3}Mg_{1/2}O_2$ synthesis

P2 $Na_{2/3}Cr_{1/3}Mg_{1/6}Ti_{1/2}O_2$ was prepared from Na_2CO_3 (99.5%, Wako Pure Chemical Industries, Ltd), Cr_2O_3 (98%, Wako Pure Chemical Industries, Ltd), $Mg(OH)_2$ (Wako Pure Chemical Industries, Ltd) and anatase TiO_2 (98.5%, Wako Pure Chemical Industries, Ltd). An excess amount (3 mol%) of Na_2CO_3 was used to compensate for the vaporization of Na ions. These precursors were thoroughly mixed by wet ball-milling with a ZrO_2 pot (40 mL), balls (27 g), and ethanol (20 mL). After drying ethanol, the mixture was pelletized at a pressure of 15 MPa. The pellets were placed on an alumina boat and were heated in a tube furnace at 1000 °C for 5 h. Finally, the sample was hand-milled before electrode preparation. The obtained powder displayed a green color.

P2 $Na_{0.67}Li_{0.22}Ti_{0.78}O_2$ synthesis

P2 $Na_{0.67}Li_{0.22}Ti_{0.78}O_2$ was prepared from Na_2CO_3 (99.5%, Wako Pure Chemical Industries, Ltd), LiOH (98%, Wako Pure Chemical Industries, Ltd), and anatase TiO_2 (98.5%, Wako Pure Chemical Industries, Ltd). The precursors were thoroughly mixed by wet ball-milling with a ZrO_2 pot (40 mL) and balls (27 g) with ethanol (20 mL) at 300 rpm for 5 h in air. Afterward, the obtained powder was pressed into a pellet at a pressure of 15 MPa and heated in a tube furnace at 850 °C under an argon atmosphere for 20 hours. Finally, the sample was hand-milled before electrode preparation. The powder displayed a light-yellow color.

Soaking treatment in water

The as-prepared samples were soaked in 50 mL of distilled water for 3 hours. Afterward, the powder was filtered and washed with an additional 50 mL of distilled water. The filtered powder was dried in a vacuum at 60 °C for 3 hours, and the obtained powder was labeled as SK-"sample name". Powder samples preserved their original colors. The filtered distilled water was evaporated at 100 °C, forming a white powder. The samples were stored in a N_2 filled glove box.

Moistening treatment

The as-prepared samples were exposed to a moisturized chamber with a relative humidity (RH) of 100% for 5 days. The as-obtained powder was labeled as RH-"sample name". The powder samples preserved their original colors after the moisture exposure test. The samples were dried in a vacuum at 60 °C for 3 hours and stored in a N_2 filled glove box.

Post-calcination treatment

After soaking or moistening treatments, the powder was again pelletized and calcined at a fixed temperature in the range 300–1000 °C for 5 hours. The as-obtained sample was labeled as SK-calcined or RH-calcined, respectively. Powder samples preserved their original colors. Finally, the sample was hand-milled to form a powder before electrode preparation.

Electrochemical evaluation

Composite electrodes consisted of 88 wt% active materials, 10 wt% acetylene black, and 6.3 wt% PVA-*g*-PAN, and aluminum served as a current collector. In the case of P2 $Na_{0.67}Li_{0.22}Ti_{0.78}O_2$, the ratio was 85, 10, and 5 wt%, respectively. Metallic sodium was used as a counter electrode. The electrolyte solution used was 1.0 mol dm^{-3} $NaPF_6$ dissolved in propylene carbonate (Kishida Chemical, battery grade). A glass filter (GB-100R, Advantec) was used as a separator. Two-electrode cells (TJ-AC, Tomcell Japan) were assembled in an argon-filled glovebox.

Characterization

Particle morphology of the samples was observed using a scanning electron microscope coupled with an energy-dispersive X-ray spectrometer (SEM-EDS) (JCM-6000, JEOL). X-ray diffraction (XRD) patterns of the samples were collected using an X-ray diffractometer (D2 PHASER; Bruker Corp., Ltd) equipped with a one-dimensional X-ray detector using Cu Kα radiation generated at 300 W (30 kV and 10 mA) with a Ni filter. The attenuated total reflectance Fourier-transform infrared (ATR-FTIR) spectra were collected on a FTIR-6200 spectrometer (Jasco). The UV-vis spectra were collected on a V-560 (JASCO).

Data availability

All relevant experimental and theoretical data within the article will be provided by the corresponding author on reasonable request.

Author contributions

Y. N. conceived the project, designed the experiments and supervised the manuscript writing. B. D. L. C. conducted the experimental work and wrote the original manuscript. T. I. and K. T. synthesized, characterized, and electrochemically evaluated the electrode materials. All authors analyzed the data and contributed to the review of the manuscript.

Conflicts of interest

The authors declare no competing financial interest.

Acknowledgements

FT-IR spectroscopy was carried out using a FTIR-6200 (JASCO Corporation), and UV-vis spectroscopy was carried out using a V-560 (JASCO Corporation) at the Instrumental Analysis Center at Yokohama National University. NY acknowledges the partial support from JSPS, Grant-in-Aid for Scientific Research (Grant Numbers 21H04698 and 23K17954). This work was also partially supported by JST, CREST Grant Number JPMJCR21O6, Japan. This work was in part supported by the MEXT Program: Data Creation and Utilization Type Materials Research and Development Project (Grant Number JPMXP1121467561). NY acknowledges the partial support by JST as part of Adopting Sustainable Partnerships for Innovative Research Ecosystem (ASPIRE), Grant Number JPMJAP2313. This work was also partially supported by JST, Grant Numbers JPMJPF2016 and JPMJMS2282-13.

References

1 P. Denholm, E. Ela, B. Kirby and M. Milligan, *The Role of Energy Storage with Renewable Electricity Generation*, 2010, **https://www.nrel.gov/docs/fy10osti/47187.pdf**.

2 M. Arbabzadeh, R. Sioshansi, J. X. Johnson and G. A. Keoleian, *Nat. Commun.*, 2019, **10**, 3413.

3 D. Reber, S. R. Jarvis and M. P. Marshak, *Energy Adv.*, 2023, **2**, 1357–1365.

4 P. C. Böttcher, L. Rydin Gorjão, C. Beck, R. Jumar, H. Maass, V. Hagenmeyer, D. Witthaut and B. Schäfer, *Energy Adv.*, 2023, **2**, 91–97.

5 M. H. Barecka and J. W. Ager, *Energy Adv.*, 2023, **2**, 268–279.

6 P. Mao, H. Arandiyan, S. S. Mofarah, P. Koshy, C. Pozo-Gonzalo, R. Zheng, Z. Wang, Y. Wang, S. K. Bhargava, H. Sun, Z. Shao and Y. Liu, *Energy Adv.*, 2023, **2**, 465–502.

7 T. Sato, K. Yoshikawa, W. Zhao, T. Kobayashi, H. B. Rajendra, M. Yonemura and N. Yabuuchi, *Energy Mater. Adv.*, 2021, **2021**, 9857563.

8 N. Yabuuchi, K. Kubota, M. Dahbi and S. Komaba, *Chem. Rev.*, 2014, **114**, 11636–11682.

9 L. Mauler, X. Lou, F. Duffner and J. Leker, *Energy Adv.*, 2022, **1**, 136–145.

10 B. D. L. Campéon and N. Yabuuchi, *Chem. Phys. Rev.*, 2021, **2**, 041306.

11 C. Ding, T. Nohira and R. Hagiwara, *Phys. Chem. Chem. Phys.*, 2016, **18**, 30770–30776.

12 A. Ponrouch, A. R. Goñi and M. R. Palacín, *Electrochem. Commun.*, 2013, **27**, 85–88.

13 A. Beda, C. Vaulot, F. Rabuel, M. Morcrette and C. Matei Ghimbeu, *Energy Adv.*, 2022, **1**, 185–190.

14 L. David, R. Bhandavat and G. Singh, *ACS Nano*, 2014, **8**, 1759–1770.

15 B. D. L. Campéon, C. Wang and Y. Nishina, *Nanoscale*, 2020, **12**, 21780–21787.

16 S. Shimizu, H. B. Rajendra, R. Watanuki and N. Yabuuchi, *Electrochemistry*, 2019, **87**, 276–280.

17 Y. Morikawa, Y. Yamada, K. Doi, S.-i. Nishimura and A. Yamada, *Electrochemistry*, 2020, **88**, 151–156.

18 Y. Fujii, R. Tatara, D. Igarashi, T. Hosaka, R. Takaishi, E. Shiiyama, T. Matsuyama and S. Komaba, *Electrochemistry*, 2023, **91**, 077002.

19 S. Kaushik, K. Matsumoto and R. Hagiwara, *Electrochemistry*, 2023, **91**, 017003.

20 Y. Wang, R. Xiao, Y.-S. Hu, M. Avdeev and L. Chen, *Nat. Commun.*, 2015, **6**, 6954.

21 C. Zhao, M. Avdeev, L. Chen and Y.-S. Hu, *Angew. Chem.*, 2018, **57**, 7056–7060.

22 R. Umezawa, Y. Tsuchiya, T. Ishigaki, H. B. Rajendra and N. Yabuuchi, *Chem. Commun.*, 2021, **57**, 2756–2759.

23 Q. Ding, W. Zheng, A. Zhao, Y. Zhao, K. Chen, X. Zhou, H. Zhang, Q. Li, X. Ai, H. Yang, Y. Fang and Y. Cao, *Adv. Energy Mater.*, 2023, **13**, 2203802.

24 Y. You, A. Dolocan, W. Li and A. Manthiram, *Nano Lett.*, 2019, **19**, 182–188.

25 K. Kubota and S. Komaba, *J. Electrochem. Soc.*, 2015, **162**, A2538.

26 S.-H. Bo, X. Li, A. J. Toumar and G. Ceder, *Chem. Mater.*, 2016, **28**, 1419–1429.

27 W. Zuo, J. Qiu, X. Liu, F. Ren, H. Liu, H. He, C. Luo, J. Li, G. F. Ortiz, H. Duan, J. Liu, M.-S. Wang, Y. Li, R. Fu and Y. Yang, *Nat. Commun.*, 2020, **11**, 3544.

28 Y. Tsuchiya, K. Takanashi, T. Nishinobo, A. Hokura, M. Yonemura, T. Matsukawa, T. Ishigaki, K. Yamanaka, T. Ohta and N. Yabuuchi, *Chem. Mater.*, 2016, **28**, 7006–7016.

29 Y. Wang, X. Yu, S. Xu, J. Bai, R. Xiao, Y.-S. Hu, H. Li, X.-Q. Yang, L. Chen and X. Huang, *Nat. Commun.*, 2013, **4**, 2365.

30 C. Delmas, C. Fouassier and P. Hagenmuller, *Physica B+C*, 1980, **99**, 81–85.

31 V. Duffort, E. Talaie, R. Black and L. F. Nazar, *Chem. Mater.*, 2015, **27**, 2515–2524.

32 R. S. Gärtner, M. M. Seckler and G.-J. Witkamp, *J. Chem. Eng. Data*, 2004, **49**, 116–125.

33 Y. Foucaud, M. Badawi, L. O. Filippov, O. Barres, I. V. Filippova and S. Lebègue, *Chem. Sci.*, 2019, **10**, 9928–9940.

34 W. Zuo, Z. Xiao, M. Zarrabeitia, X. Xue, Y. Yang and S. Passerini, *ACS Mater. Lett.*, 2022, **4**, 1074–1086.

35 Y. Michiue, *J. Solid State Chem.*, 2006, **179**, 2578–2583.

36 B. D. L. Campéon, R. Umezawa, A. K. Pandey, T. Ishikawa, Y. Tsuchiya, Y. Ishigaki, R. Kanto and N. Yabuuchi, *ACS Appl. Mater. Interfaces*, 2024, **16**, 3396–3405.

37 M. F. Rabuni, N. M. Nik Sulaiman, M. K. Aroua and N. A. Hashim, *Ind. Eng. Chem. Res.*, 2013, **52**, 15874–15882.

38 S. Roberts, L. Chen, B. Kishore, C. E. J. Dancer, M. J. H. Simmons and E. Kendrick, *J. Colloid Interface Sci.*, 2022, **627**, 427–437.

39 G. J. Ross, J. F. Watts, M. P. Hill and P. Morrissey, *Polymer*, 2000, **41**, 1685–1696.

40 I. Konuma, Y. Ugata and N. Yabuuchi, *Energy Adv.*, 2024, **3**, 962–967.